International Journal of Heat and Fluid Flow 29 (2008) 1268–1278

Contents lists available at ScienceDirect

International Journal of Heat and Fluid Flow

journal homepage: www.elsevier.com/locate/ijhff

Flow field characterization of a rotating cylinder

Jong-Yeon Hwang [a], Kyung-Soo Yang [b,*], Dong-Hyeog Yoon [b], Klaus Bremhorst [c]

[a] CEM R&E Project Department, POSCO, Pohang 790-785, Republic of Korea
[b] Department of Mechanical Engineering, Inha University, Incheon 402-751, Republic of Korea
[c] Department of Mechanical Engineering, The University of Queensland, Brisbane, Qld 4072, Australia

ARTICLE INFO

Article history:
Received 12 August 2007
Received in revised form 7 April 2008
Accepted 24 April 2008
Available online 12 June 2008

Keywords:
Circular cylinder
Coriolis force
Direct numerical simulation
Turbulent flow
Wall shear stress

ABSTRACT

Direct numerical simulation is used to study the flow field around an infinitely long circular cylinder rotating in fluid with no outer boundary. Wall shear stresses and normal pressure fluctuations are considered with reference to flat, non-rotating geometries to help identify any flow field differences introduced by Coriolis forces. In the present case, Coriolis forces are experienced only by the turbulence field. The dominant effect is to decrease the streamwise turbulent velocity level relative to the other two components. A consequential effect is that the two components of wall shear stress fluctuations become almost equal and spectra for streamwise and spanwise wall shear stress fluctuations become almost identical. This is a distinctly different behaviour from that of non-rotating flat plate and straight pipe flows. Instantaneous wall shear stress fluctuations indicate a near wall flow structure similar to that of other boundary layers with sweeps and ejections. No flow reversals of wall shear stress are indicated. A good correlation of the wall shear stresses and the turbulent kinetic energy exists for $y^+ < 10$. Budgets of Reynolds normal stress components illustrate the role played by Coriolis forces in the production and redistribution of turbulence energies. Wall pressure fluctuations are found to be of much larger spatial extent than velocity fluctuation scales while the probability density distribution of pressure fluctuations is almost Gaussian but does display a Reynolds number effect for skewness and Kurtosis. The ratio of rms pressure fluctuations to mean streamwise wall shear stress follows closely that for flat plate boundary layer and channel flows.

1. Introduction

Rotating circular cylinders are widely used for laboratory assessment of the effect of fluid velocity on corrosion rates (Gabe, 1974; Gabe and Walsh, 1983; Silverman, 1988; Nesic et al., 1995; Gabe et al., 1998). Applications can also be found in viscosity determination devices, biological applications (Haut et al., 2003), determination of windage losses in rotating machinery and in desalinators (Wild et al., 1996). Theoretical solutions relating the mass transfer to the flow around the cylinder are covered in texts such as Levich (1962), Pletcher and Walsh (1993) and Hanratty and Campbell (1996). Corrosion rates obtained with the rotating electrode apparatus are transferred to industrial applications in pipe and duct flows, behind obstacles and for external flows (Levich, 1962; Nesic and Postlethwaite, 1990; Nesic et al., 1995, 1997; Darby et al., 1999; Silverman, 2003). Since the fluid in such situations is usually of high Schmidt number, typically greater than 1000, the mass transfer boundary layer, or diffusion layer, is very thin and in typical boundary layers, lies largely within the viscous sublayer. This assumption justifies the transfer of mass transfer controlled corrosion data to other flows on the basis of similar mean wall shear stress. As has already been shown by Levich (1962), Nesic and Postlethwaite (1990) and others, this is not a universally correct process especially in separated flows with downstream reattachment where the mean wall shear stress vanishes at the flow reattachment point yet mass transfer and corrosion rates in the region of reattachment do not vanish (Bremhorst et al., 2005).

While many experimental as well as numerical studies exist for boundary layer flows in channels, in pipes and over flat surfaces from which the structure of turbulent flow can be deduced, few studies exist for the rotating cylinder. Theodorsen and Reiger (1944) are one of the first to give rotating cylinder wall shear stress for a comprehensive set of experimental data while Pettersson et al. (1996) and Dierich et al. (1998) report detailed hot-wire anemometer data for flow near a rotating cylinder of geometry similar to that used for rotating electrodes. Pettersson et al. (1996) and also Jacobs et al. (2006) attempted to predict the flow field around the rotating cylinder by application of Reynolds averaged modelling but demonstrate only limited success. Kasagi and Hirata (1975) experimentally studied turbulent fluid motions and heat transfer in the near wall region of a rotating circular cylinder,

* Corresponding author. Tel.: +82 32 860 7322; fax: +82 32 868 1716.
E-mail address: ksyang@inha.ac.kr (K.-S. Yang).

0142-727X/$ - see front matter © 2008 Elsevier Inc. All rights reserved.
doi:10.1016/j.ijheatfluidflow.2008.04.008

Nomenclature

D [m]	cylinder diameter
f [–]	friction factor
L_s^+ [–]	integral length scale in the streamwise direction in wall unit
L_z^+ [–]	integral length scale in the spanwise direction in wall unit
R [m]	cylinder radius
Re_D [–]	Reynolds number based on cylinder diameter and the surface velocity of the cylinder ($2R^2\Omega/\nu$)
Re_R [–]	Reynolds number based on cylinder radius and the surface velocity of the cylinder ($R^2\Omega/\nu$)
Re^*_R [–]	Reynolds number based on friction velocity and cylinder radius (u^*R/ν)
Re_τ [–]	Reynolds number based on friction velocity and channel half width or boundary layer thickness
r [m]	radial coordinate
s [m]	streamwise (circumferential) coordinate
t [s]	time
U_c [m/s]	velocity at the cylinder surface ($R\Omega$)
u [m/s]	streamwise velocity component
u^+ [–]	normalized streamwise (circumferential) velocity component (u/u^*)
u^* [m/s]	friction velocity ($\sqrt{\overline{\tau_{w,s}}/\rho}$)
v [m/s]	radial (normal) velocity component
w [m/s]	spanwise velocity component
y^+ [–]	normalized distance from the wall (yu^*/ν)
y [m]	distance from the wall
z [m]	spanwise coordinate

Greek letters

ϕ [–]	probability density
μ [kg/m s]	dynamic viscosity
ν [m^2/s]	kinematic viscosity
ρ [kg/m^3]	density
τ_w [Pa]	total wall shear stress
$\tau_{w,s}$ [Pa]	streamwise component of wall shear stress
$\tau_{w,z}$ [Pa]	spanwise component of wall shear stress
$\vec{\Omega}$ [s^{-1}]	angular velocity vector of the cylinder, $\vec{\Omega} = -\Omega\vec{k}$

Superscripts

$\bar{}$	time and spatial averaged quantity
$'$	fluctuating value
$\rightarrow$	vector notation

Other symbol

$\langle\ \rangle$	rms averaged quantity

and report that these fluid motions consist of the ejection of the high-speed portion of the fluid near the wall and the subsequent supply of the low-speed fluid inward to the wall.

Corrosion can also be induced by mechanical damage to the protective layer such as an oxide of the base metal. Such damage is well understood when a solid phase is present in the liquid stream but little is known about mechanical failure due to fluctuating pressure and shear forces and in particular possible fatigue induced by the associated rapidly fluctuating forces. These forces are difficult to measure but are readily accessible by computation using direct numerical simulation (DNS) of the flow equations. While such calculations exist for straight pipe and flat plate boundary layer flow, comparable data are sparse for the rotating cylinder where the flow field is known to differ from flat, non-rotating geometries due to the presence of Coriolis forces (Hwang et al., 2007). Coriolis forces reduce the streamwise velocity fluctuations relative to the wall normal and lateral ones, a fact also observed in parts of rotating channel flows (Launder et al., 1987; Kristoffersen and Andersson, 1993). Consequently, it is of interest to quantify the rotating cylinder wall forces and flow characteristics in case these lead to different corrosion behaviour on the rotating cylinder relative to that of flat plate boundary layer, channel and pipe flows. The present paper presents such data for fluctuating wall shear stress and wall pressure fluctuation for a smooth rotating cylinder of infinite extent with no outer boundary.

2. Formulation and numerical methods

The geometry, numerical method and parameters are the same as those used by Hwang et al. (2007) and are repeated here for completeness. The governing incompressible continuity and momentum equations in a reference frame rotating at constant angular velocity ($\vec{\Omega}$) with the cylinder are

$$\vec{\nabla}\cdot\vec{u} = 0, \tag{1}$$

$$\frac{\partial\vec{u}}{\partial t} + (\vec{u}\cdot\vec{\nabla})\vec{u} = -\frac{1}{\rho}\vec{\nabla}P + \nu\vec{\nabla}^2\vec{u} - 2\vec{\Omega}\times\vec{u}, \tag{2}$$

where $\vec{u}$, ρ and ν denote velocity, density, and kinematic viscosity of the fluid, respectively. The last term in Eq. (2) represents the Coriolis force. Since the centrifugal force is conservative, it is included in the pressure term, and does not affect the velocity field (Lezius and Johnston, 1976). Thus, P in Eq. (2) actually includes not only pressure but also the centrifugal potential.

The governing equations are discretized by using a finite-volume method on a cylindrical grid system. Spatial discretization is second-order accurate. A hybrid scheme is used for time advancement; non-linear terms are explicitly advanced by a third-order Runge–Kutta scheme, and the other terms are implicitly advanced by the Crank–Nicolson scheme. A fractional step method (Rosenfeld et al., 1994), is employed to decouple the continuity and momentum equations. The resulting Poisson equation is solved by a multigrid method. Details of the numerical algorithm used in the code follow Rosenfeld et al. (1994).

3. Choice of parameters and boundary conditions

A schematic of the flow configuration under consideration is shown in Fig. 1 together with the coordinate system employed. A circular cylinder rotates in the clockwise direction in an open domain. The cylinder radius is 0.01 m, and the outer boundary of the computational domain is located 0.07 m from the axis of rotation. The spanwise size of the domain is 0.024 m at rpm = 200 and 500, and 0.012 m at rpm = 1000. The spanwise length is large enough to contain the longest wavelength of turbulence in the spanwise direction. A cylindrical grid system is employed, and the number of computational cells determined by grid refinement study is $128 \times 96 \times 256$ in the azimuthal (s), radial (r or y) and spanwise (z) directions, respectively. The minimum grid sizes in the s and r directions are $\Delta s^+_{\min} = 17.8$ and $\Delta r^+_{\min} = 0.09$, respectively, for rpm = 500; the grid size in the z direction is $\Delta z^+ = 3.3$ ($\Delta z^+ = 2.9$ for rpm = 1000). They are quite small as verified for adequacy by grid refinement. A periodic boundary condition is employed in the homogeneous spanwise direction. The outer boundary condition needs special attention. To minimize computa-

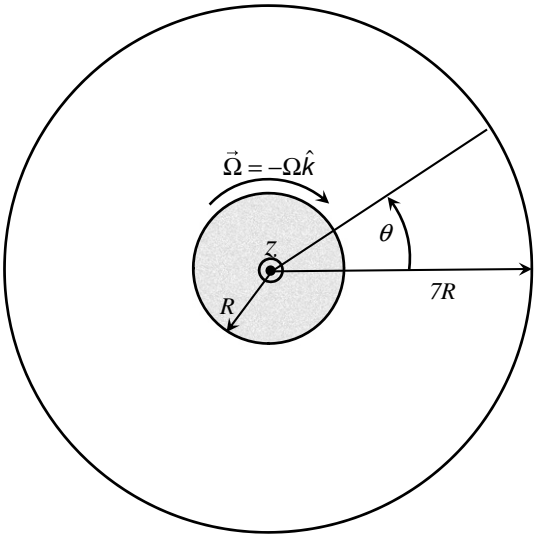

Fig. 1. Schematic of flow configuration and coordinate system. Here, Ω is positive.

Table 1
Mean flow parameters

rpm	U_c (m/s)	u^* (m/s)	Re_R	Re_R^*	$\sqrt{\overline{\tau_{w,s}^2}}/\overline{\tau_{w,s}}$	$\sqrt{\overline{\tau_{w,z}^2}}/\overline{\tau_{w,s}}$	$\sqrt{\overline{\tau_w^2}}/\overline{\tau_{w,s}}$
200	0.21	0.019	1810	161	0.26	0.27	0.374
500	0.52	0.040	4480	348	0.295	0.295	0.417
1000	1.05	0.072	9050	623	0.32	0.305	0.442

tional costs, the boundary condition as suggested by Yang et al. (2003) is employed. That is

$$\frac{\partial u}{\partial r} = \Omega, \qquad v = 0, \qquad \frac{\partial w}{\partial r} = 0, \tag{3}$$

where u, v and w represent the azimuthal, normal and spanwise velocity components, respectively. This outer boundary condition enables use of a reasonably small computational domain in the radial direction. The use of this boundary condition contrasts with the shear outer boundary which leads to vortical flows in the enclosed space. The advantage of the present outer boundary condition is that no shear effects are generated at that boundary. Table 1 shows the computed mean flow parameters, where U_c and u^* denote the velocity at the cylinder surface and the friction velocity, respectively. Re_R is the Reynolds number based on the cylinder radius R and U_c while Re_R^* is based on R and u^*. As the transitional Re_R is 100 (Theodorsen and Reiger, 1944; Gabe and Walsh, 1983), the flows at all three Reynolds numbers are expected to be fully turbulent.

To justify the computational domain size, an additional simulation with a larger computational domain ($L = 13R$, here, L denotes the radius of the outer boundary) was performed. More grid cells were added ($128 \times 128 \times 256$ in total) such that the original level of numerical resolution was maintained in the new simulation. The budgets of Reynolds normal stresses computed with the larger domain are almost indistinguishable from those with the original domain ($L = 7R$) thus confirming the adequacy of the smaller computational domain ($L = 7R$). In both cases, turbulence almost completely decays within $3R$ ($y^+ \sim 1000$). The adequacy of the streamwise resolution was checked by performing an additional simulation with the doubled number of grid cells in the streamwise (circumferential) direction and $L = 7R$. The budgets of Reynolds normal stresses were computed with the finer resolution. The difference between the two cases is insignificant, confirming that the coarser streamwise resolution is adequate.

4. Results and discussion

4.1. Mean velocity profiles and boundary layer parameters

Based on the coordinate system rotating with the cylinder, velocities are relative to the wall with a no slip condition. Hwang et al. (2007) have shown that in the fully turbulent layer a logarithmic velocity profile exists, Fig. 2. The slope is the same as the universal velocity profile applicable for flat plate boundary layers and channel and straight pipe flows, Eq. (4), before limiting to the rigid body velocity profile at larger distances from the cylinder wall

$$u^+ = 2.5 \ln y^+ + 5.5. \tag{4}$$

The logarithmic profile is, however, offset relative to the universal velocity one due to a thinner wall layer with the constant in the log law being 2.65 instead of 5.5. The data of Dierich et al. (1998) are shown replotted in Fig. 2 for the lowest and highest rotational speeds reported. It is seen that once again a logarithmic region with the same slope as the DNS data is obtained and lying well below the universal velocity profile, with the constant 5.5 of the universal velocity profile being replaced by −0.75.

The values of 99% boundary layer thickness (δ_{99}), displacement thickness (δ^*), momentum thickness (θ), and shape factor (H) at $Re_R^* = 348$ are also presented in Table 2. They were computed as follows where δ_{99} is normal distance between the cylinder surface and the y location of $U/U_0 \approx 0.99$

$$\delta^* = \int_R^{7R} \left(1 - \frac{U}{U_0}\right) dr,$$
$$\theta = \int_R^{7R} \frac{U}{U_0}\left(1 - \frac{U}{U_0}\right) dr,$$
$$H = \delta^*/\theta,$$

where $U = u - r\Omega + U_0$ with $U_0 = R\Omega$.

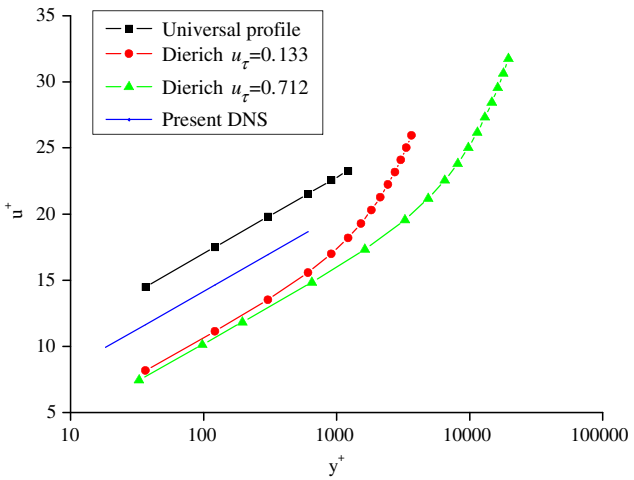

Fig. 2. Mean velocity profiles in the wall region relative to a reference frame rotating with the cylinder.

Table 2
Boundary layer thicknesses for the mean velocity profile at $Re_R^* = 348$

δ_{99}	δ^*	θ	H
3.00R	0.20R	0.16R	1.25

4.2. Mean wall shear stress variation with Reynolds number

One of the more frequently quoted sets of wall shear stress data and associated correlation is that by Theodorsen and Reiger (1944), Eq. (5), which is applicable for $1000 \leqslant \mathrm{Re}_R \leqslant 400{,}000$

$$\frac{1}{\sqrt{f}} = -0.6 + 4.07\log_{10}(\mathrm{Re}_R\sqrt{f}). \tag{5}$$

Friction factor (f) is defined by

$$\tau_w = \frac{1}{2} f \rho U_c^2. \tag{6}$$

Eisenberg et al. (1954) found their experimental data to follow

$$\frac{f}{2} \approx 0.0791 \mathrm{Re}_D^{-0.3} \tag{7}$$

for $1000 \leqslant \mathrm{Re}_D \leqslant 100{,}000$ with Reynolds number, Re_D, based on cylinder diameter.

Dierich et al. (1998) present a more limited experimental data set which lies below the trend of Eq. (5) but approaches this line as Reynolds number increases, Fig. 3. It is seen in Fig. 3 that there is a spread of the correlations and that the DNS data are within the range of experimental data. Reasons why the DNS data may not fully agree with the experimental data include the differences in distance of the outer boundary from the cylinder surface, the free end of the cylinder, possible recirculating flow and experimental errors. The ability of DNS to simulate an infinitely long cylinder thus excluding end effects and use of the boundary conditions of Eq. (3) thus removing the effects of the outer cylinder, are considered to be the most likely reason for a difference between the experimental data and the DNS points in Fig. 3. A possible reason for the Dierich et al. (1998) data differing from the Theodorsen and Reiger (1944) and Eisenberg et al. (1954) data is that wall shear stress was obtained from hot-wire anemometer measurements away from the wall by applying the assumption that viscous effects are negligible so that wall shear stress equals the turbulent Reynolds stress. Present computations show that even at the highest Reynolds number tested, the viscous component remains significant up to $y^+ = 50$ which is into the logarithmic layer of the flow. As Reynolds number decreases, the viscous component will increase in extent throughout the flow thus giving an increasing departure from the other two experimental data sets of Fig. 3. Experimental data given in Pettersson et al. (1996) are not included on Fig. 3 as they depart significantly from the other data shown with insufficient details being available to judge their comparability.

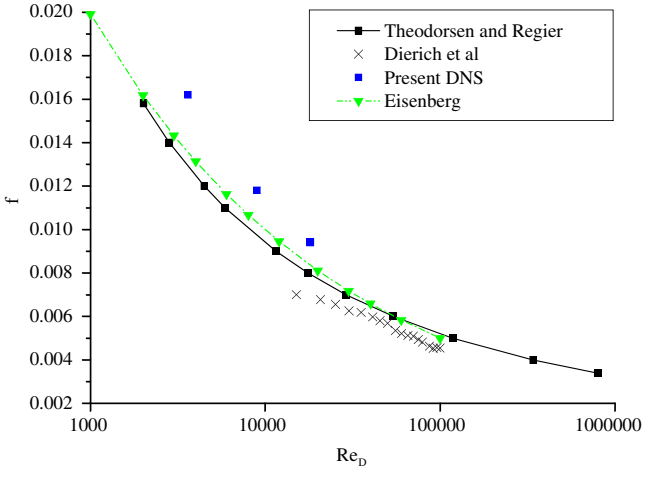

Fig. 3. Friction factor variation with Reynolds number.

4.3. Streamwise and spanwise fluctuating wall shear stresses

The two components of the fluctuating wall shear stress are defined by

$$\tau'_{w,s} = \mu r \frac{\partial}{\partial r}\frac{u'}{r}\bigg|_{r=R} \tag{8}$$

$$\tau'_{w,z} = \mu \frac{\partial w'}{\partial r}\bigg|_{r=R}, \tag{9}$$

where the superscript $'$ denotes a fluctuating component. $\tau'_{w,s}$ is that in the azimuthal or streamwise direction while $\tau'_{w,z}$ is the fluctuating component of wall shear stress in the spanwise direction. μ is the dynamic viscosity. Table 1 gives values of rms wall shear stress fluctuations relative to the mean wall shear stress which is non-zero only in the streamwise direction denoted by subscript s. The last column is the vectorial sum of the component shear stress fluctuations. The most noticeable aspect of these data is that the two components of fluctuating wall shear stress are nearly equal. This contrasts with the DNS data for a channel (Jeon et al., 1999), who give the streamwise component as 0.36 and the spanwise component as 0.2 giving a ratio of 1.8 and a vectorial sum of 0.412. As wall shear stress fluctuations are directly related to the streamwise and spanwise velocity fluctuations near the wall, it is seen from Hwang et al. (2007) that because Coriolis forces lead to a significant reduction in the streamwise near wall velocity fluctuations a lower ratio of the two components of shear stress fluctuations results. Fig. 4 presents comparison of the current rms values of fluctuating wall shear stress components with those of channel flow obtained by other authors. It is seen that the difference between the streamwise and spanwise values is significant in channel flow. However, there is only a small difference in the current flow. In all cases, the rms fluctuations increase with approximately the same rate as Reynolds number increases.

4.4. Spectra of fluctuating wall shear stress components

Spectra of fluctuating wall shear stress components were computed by Fourier transform from the corresponding spatial correlations which are available in Hwang et al. (2007). The resultant spectra, Fig. 5, differ significantly from those of non-rotating flows with negligible streamline curvature such as Colella and Keith (2003) for a flat plate and Jeon et al. (1999) for channel flow. The production part of the spectrum is similar in shape for both components and the drop off to higher wavenumbers is more rapid than for the flat plate case. Also, the shape of spectra for the two

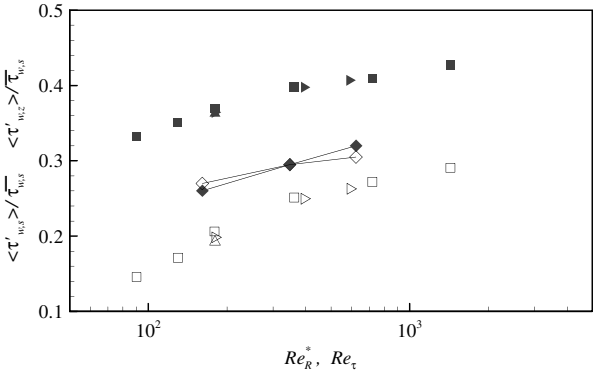

Fig. 4. rms values of fluctuating wall shear stress components normalized by the mean wall shear stress. Solid and hollow symbols denote streamwise and spanwise components, respectively. —◆—, —◇—, present; ■, □, DNS of channel flow by Hu et al. (2006); ▶, ▷, DNS of channel flow by Moser et al. (1999); ▲, △, DNS of channel flow by Kim et al. (1987).

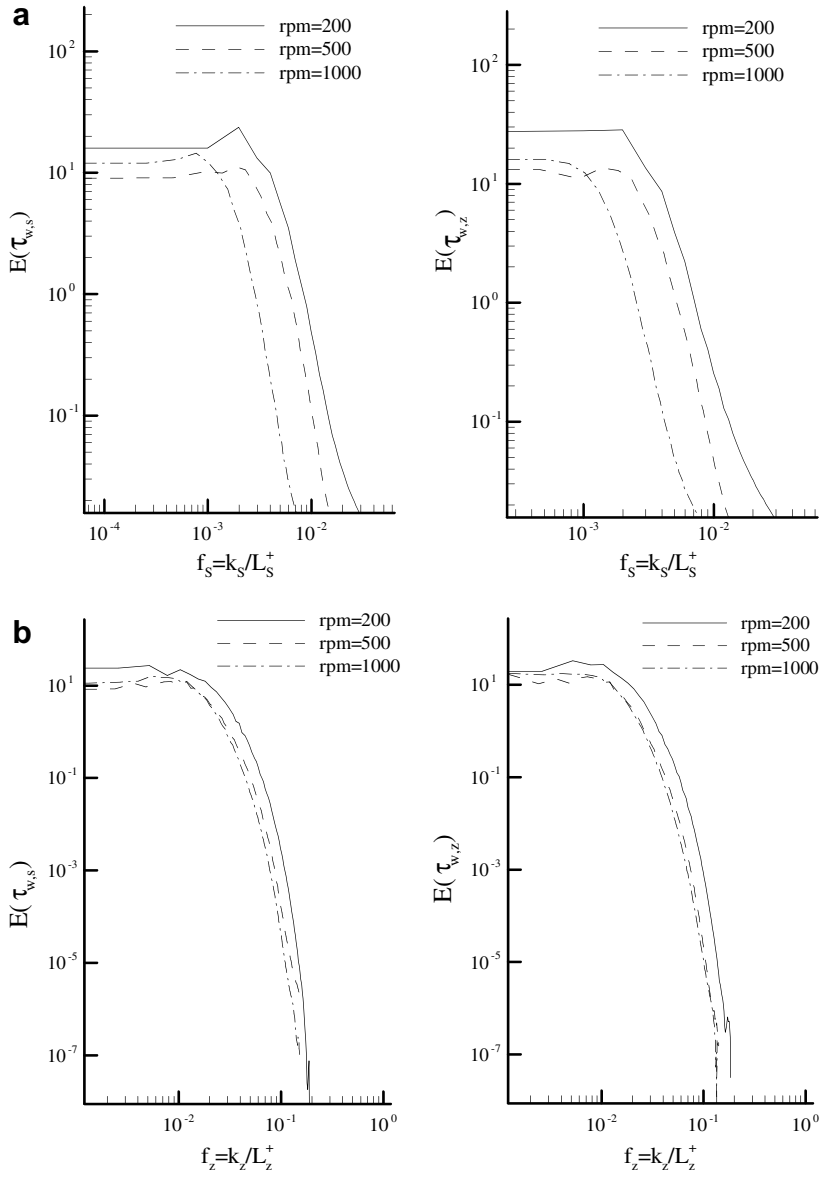

Fig. 5. Spectra of wall shear stress fluctuations obtained from spatial correlations with (a) streamwise separation and (b) spanwise separation. Integral length scale is used for normalizing the wavenumbers.

components of wall shear stress fluctuations is almost identical for each direction of separation. This is attributed to the manner in which the streamwise turbulence intensity is reduced relative to the other components under the influence of Coriolis forces (Hwang et al., 2007; Launder et al., 1987), and appears to act like an anisotropy weakening effect.

4.5. Probability density distributions of fluctuating wall shear stress components

Probability density distributions were calculated according to Eq. (10) where subscript x is replaced by s for the streamwise component and by z for the spanwise one. n is the number of samples in the interval denoted by Δ and N is the total number of samples

$$\phi(\tau'_{w,x})\Delta(\tau'_{w,x}) = \frac{n}{N}, \qquad \phi(\tau'_{w,x}) \geqslant 0, \quad \int_{-\infty}^{+\infty} \phi(\tau'_{w,x})\mathrm{d}(\tau'_{w,x}) = 1. \tag{10}$$

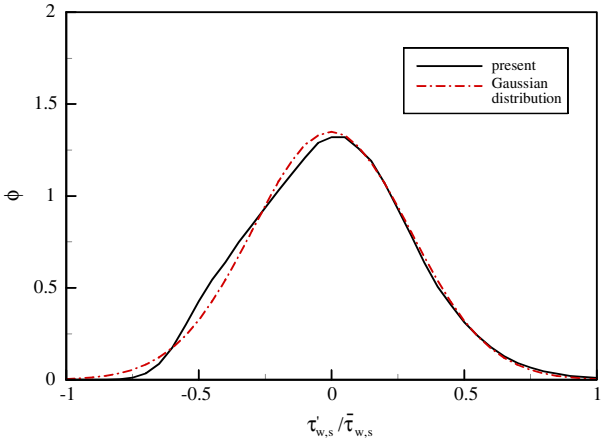

Fig. 6. Probability density function for streamwise wall shear stress fluctuation at $Re_R^* = 348$.

Their distributions are shown in Figs. 6 and 7. Corresponding values of skewness and flatness (Kurtosis) are 0.166 and 2.79 for the streamwise wall shear stress fluctuation and 0.005 and 3.06 for the spanwise wall shear stress fluctuation. The spanwise values reflect the symmetry about the plane perpendicular to the cylinder axis. The streamwise values can be compared with those measured by Colella and Keith (2003) for a towed flat plate of 0.67 and 3.41

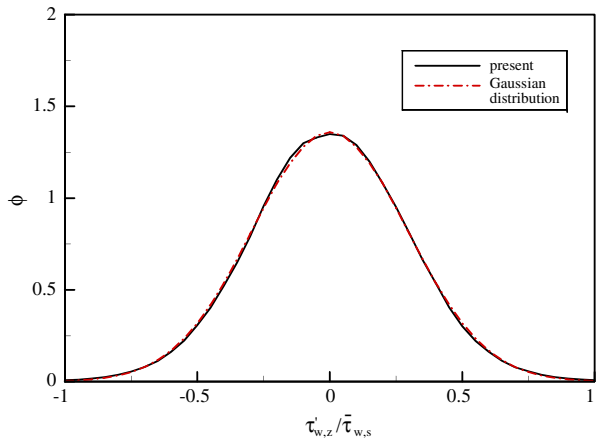

Fig. 7. Probability density function for spanwise wall shear stress fluctuation at $Re_R^* = 348$.

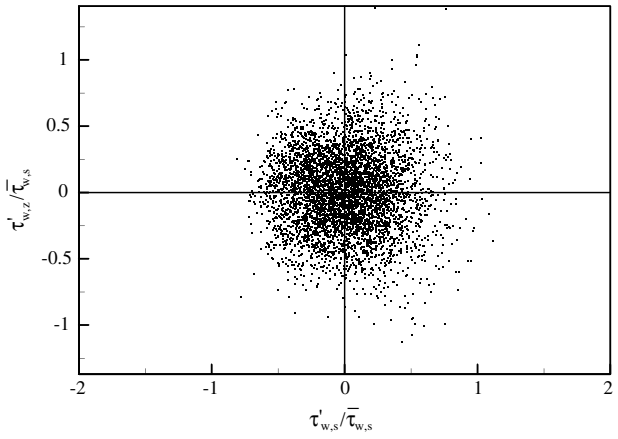

Fig. 8. Scatter plot of streamwise and spanwise wall shear stress fluctuation at $Re_R^* = 348$.

which were shown to be similar to other flat surface geometries. The significantly lower value of skewness in the present case is again attributable to the Coriolis effect which was seen to bring the two components of wall shear stress fluctuations closer together in magnitude, in spectral behaviour and now also in their probability densities.

From Fig. 8 it is deduced that the instantaneous streamwise wall shear stress never becomes negative but the positive value can exceed twice the mean wall shear stress. The spanwise fluctuation is seen to have some values exceeding the mean wall shear stress but only very rarely. Similar results were obtained by Colella and Keith (2003) for the streamwise wall shear stress fluctuation in a flat plate boundary layer at low Reynolds numbers. Fig. 8 is indicative of the lack of correlation between the two fluctuating components as is to be expected from symmetry considerations.

4.6. Characteristics of the instantaneous wall shear stress vector

The instantaneous wall shear stress vector, $\vec{\tau}_w$, is one of the mechanical forces which may affect the deposition of protective films and/or the film removal due to mechanical failure. It is defined by summation of the two wall shear stress component vectors, Eq. (11), while the magnitude is defined by Eq. (12). $\hat{i}$ and $\hat{k}$ are the unit vectors in the streamwise and spanwise directions, respectively

$$\vec{\tau}_w = \tau_{w,s}\hat{i} + \tau_{w,z}\hat{k}, \tag{11}$$

$$\tau_w = \sqrt{\tau_{w,s}^2 + \tau_{w,z}^2}. \tag{12}$$

Fig. 9 gives a plan view of instantaneous wall shear stress vectors. A definite structure can be visualized which has a longer length scale in the streamwise direction than in the spanwise one. This structure is similar in appearance to that seen in flat geometry boundary layers consisting of sweeps and ejections (Hinze, 1975). Consistent with Fig. 8, there is an absence of flow reversals as has been observed for a flat plate boundary layer by Colella and Keith (2003).

The fluctuating component of the wall shear stress vector can be analysed with the aid of the following definitions:

$$\vec{J} = \tau'_{w,s}\hat{i} + \tau'_{w,z}\hat{k} \quad J = \sqrt{\tau'^2_{w,s} + \tau'^2_{w,z}} \quad \bar{J} = \sqrt{\overline{\tau'^2_{w,s}} + \overline{\tau'^2_{w,z}}}. \tag{13}$$

The probability density of J is given in Fig. 10. The large tail of the distribution shows that fluctuations up to 1.25 times the mean shear stress exist. The maximum values of wall shear stress possible can be seen more clearly from Fig. 11 which is the probability density of the magnitude of the wall shear stress vector. The distribution is nearly Gaussian with values of up to twice the mean va-

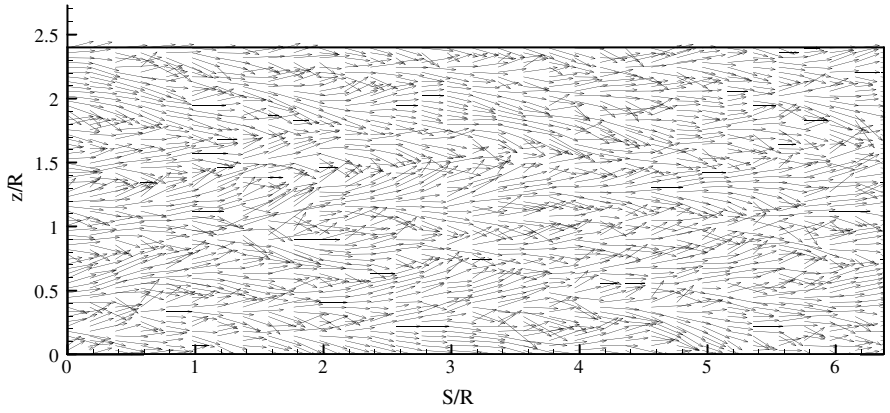

Fig. 9. Instantaneous wall shear stress vector plot in the s–z plane at $Re_R^* = 348$.

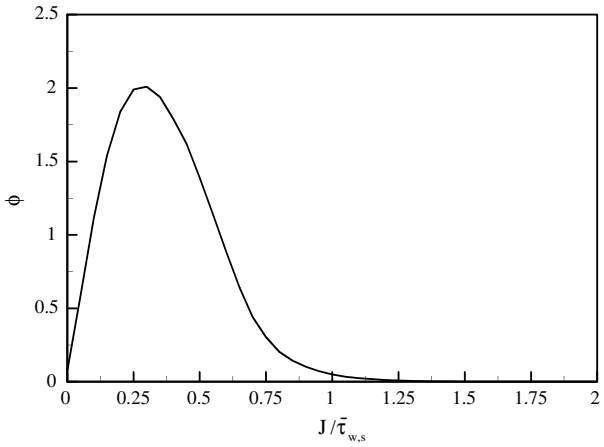

Fig. 10. Probability density function for the magnitude of wall shear stress fluctuation at $Re_R^* = 348$.

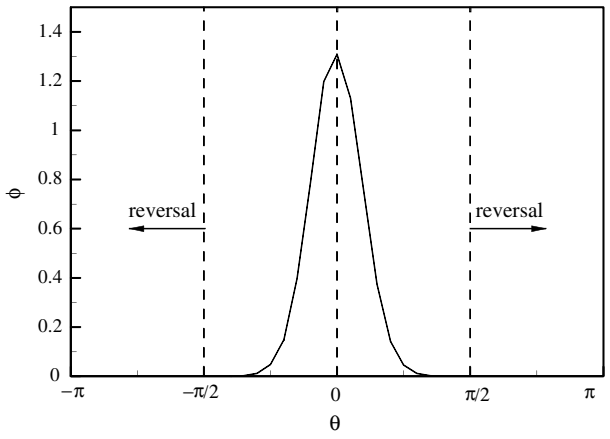

Fig. 12. Probability density function for the angle of wall shear stress vector at $Re_R^* = 348$.

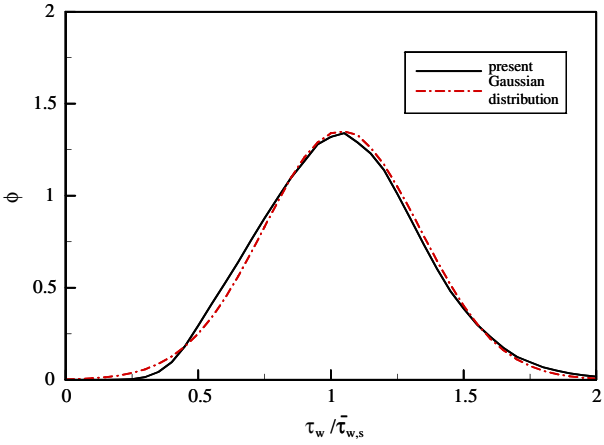

Fig. 11. Probability density function for magnitude of wall shear stress vector at $Re_R^* = 348$.

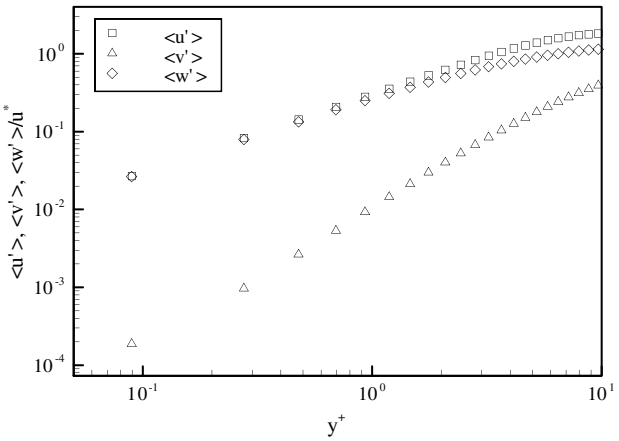

Fig. 13. Rms velocity fluctuations normalized by friction velocity in the wall region $Re_R^* = 348$.

lue. This may have significant implications when assessing flow related corrosion. The angle of the wall shear stress vector is given in Fig. 12. Limits of angles above which flow reversal would be indicated are shown and it is seen that the extreme values of the angle fall well within these limits. In fact, most vector angles are within ±45°. These results are similar to those of Colella and Keith (2003) for a flat plate boundary layer.

4.7. Role of the turbulent kinetic energy

When assessing flow assisted corrosion mean wall shear stress is considered as the primary flow variable as the diffusion layer generally lies within the viscous sublayer which in turn is characterized by wall shear stress. In turbulent flow the fluctuating wall shear stress increases the effective wall shear stress determining mass transfer and hence corrosion. The question then arises whether it is the fluctuating wall shear stress which matters or the turbulence level as given by, for example, turbulent kinetic energy.

The wall normal velocity fluctuation takes on very small values well before the wall is reached as seen from Fig. 13 which gives the individual velocity fluctuations in wall vicinity. The streamwise and spanwise rms fluctuations have the same slope near the wall, being consistent with the earlier observation that the streamwise and spanwise rms wall shear stress fluctuations are almost equal (Fig. 4). Up to $y^+ = 1, v'$ is negligible and Fig. 14 shows that the mean of the sum of squares of u' and w' is nearly identical to twice the turbulent kinetic energy up to at least $y^+ = 10$. As the fluctuating wall shear stress components are directly proportional to u' and w', this result shows that rms turbulent wall shear stress fluctuation levels can be readily predicted if accurate predictions of k within the near wall region are available.

Fig. 15 tests the correlation between $k_i = 1/2(u'^2 + v'^2 + w'^2)$ and J where k_i is the instantaneous turbulent kinetic energy. At very low y^+ a near perfect correlation is seen to exist, however, as y^+ increases, but still at $y^+ \ll 10$, the correlation breaks down at small values of velocity and wall shear stress fluctuations. This is probably due to the smaller length scale fluctuations which are associated with sweeps of low velocity fluid back towards the wall compared with the larger scale ones associated with ejections of high velocity fluid that penetrate the whole wall layer. The existence of such sweeps and ejections has already been demonstrated by Kasagi and Hirata (1975). The lack of perfect correlation at the smaller scales on the approximation of $2k \approx \overline{u'^2} + \overline{w'^2}$ is, however, negligible up to at least $y^+ = 10$.

4.8. Linearity of velocity profile and Nernst diffusion layer

Mass transfer models for high Schmidt number fluids often rely on the mass diffusion layer lying fully within the viscous sublayer, that is, within a region where the velocity profile is linear

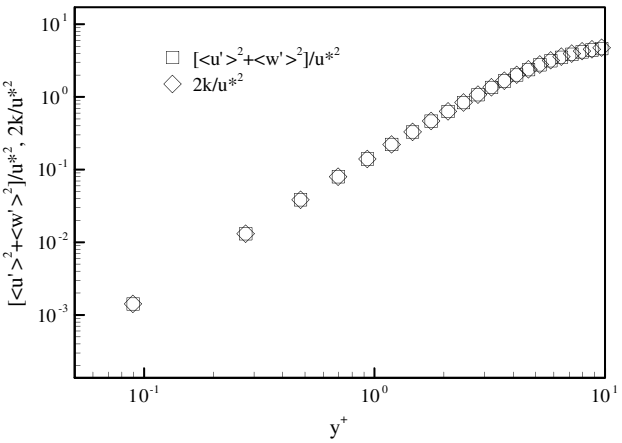

Fig. 14. Comparison between $\overline{u'^2} + \overline{w'^2}$ and $2k$ in the wall region at $Re_R^* = 348$.

(Hanratty and Campbell, 1996). It is of interest, therefore, to examine and quantify the probability that a linear profile exists which satisfies the viscous velocity profile $u^+ = y^+$ within a given accuracy. One method of presenting such data is given in Fig. 16 from which it is readily seen that within the viscous sublayer, $y^+ \leqslant 5$, the probability of $u^+ - y^+$ is centred around zero but outside of the viscous sublayer, the peak departs from zero significantly with most occurrences being skewed to below zero. The latter reflects the curvature of the velocity profile increasing as y^+ increases. The wide spread of $u^+ - y^+$ within the viscous sublayer reflects the sweep and ejection process described in the previous section and is consistent with such processes in a flat plate boundary layer (Hinze, 1975).

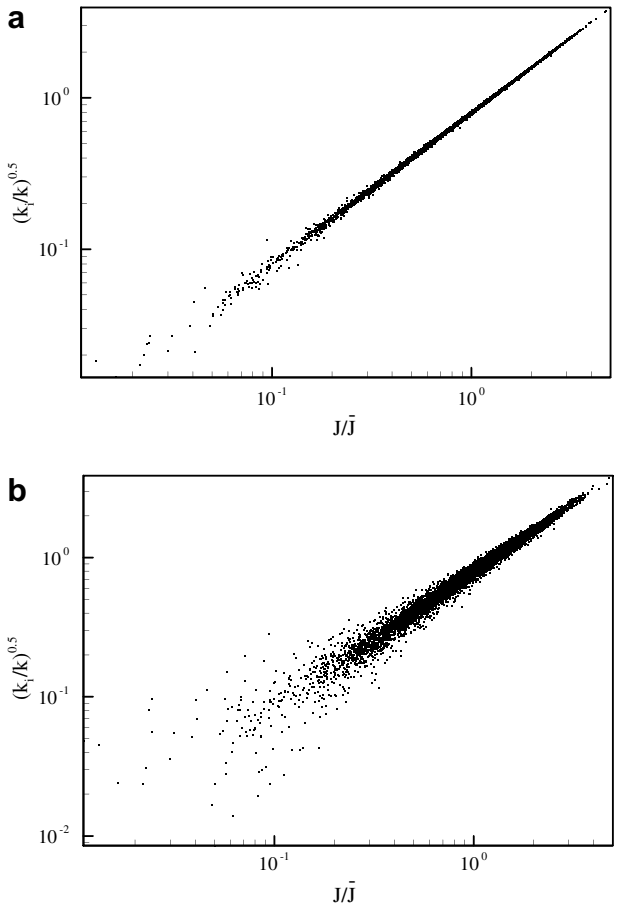

Fig. 15. Correlation between the fluctuation of wall shear stress and turbulent kinetic energy for $Re_R^* = 348$: (a) $y^+ = 0.1$ and (b) $y^+ = 1.0$.

4.9. Budgets of Reynolds normal stress components

Budgets of the transport equations for Reynolds normal stress components are given by

$\overline{u'^2}$ − budget

$$0 = \underbrace{-2\left[\overline{u'v'}\frac{dU}{dr} + \frac{\overline{u'v'}}{r}U\right]}_{P_{11}} \underbrace{-\left[\frac{1}{r}\frac{\partial r\overline{u'u'v'}}{\partial r} + \frac{2\overline{u'u'v'}}{r}\right]}_{T_{11}} + \underbrace{\nu\left[\frac{1}{r}\frac{\partial}{\partial r}\left(r\frac{\partial\overline{u'u'}}{\partial r}\right) + \frac{2}{r^2}(\overline{v'^2} - \overline{u'^2})\right]}_{D_{11}} \underbrace{-\frac{2}{\rho r}\overline{u'\frac{\partial p'}{\partial\theta}}}_{\Pi_{11}} + \underbrace{4\Omega\overline{u'v'}}_{C_{11}} - \underbrace{2\nu\left[\overline{\left(\frac{\partial u'}{\partial\theta} + v'\right)^2}\frac{1}{r^2} + \overline{\left(\frac{\partial u'}{\partial r}\right)^2} + \overline{\left(\frac{\partial u'}{\partial z}\right)^2}\right]}_{\varepsilon_{11}} \tag{14}$$

$\overline{v'^2}$ − budget

$$0 = \underbrace{4\frac{\overline{u'v'}}{r}U}_{P_{22}} \underbrace{-\left[\frac{1}{r}\frac{\partial r\overline{v'v'v'}}{\partial r} - \frac{2\overline{u'u'v'}}{r}\right]}_{T_{22}} + \underbrace{\nu\left[\frac{1}{r}\frac{\partial}{\partial r}\left(r\frac{\partial\overline{v'v'}}{\partial r}\right) + \frac{2}{r^2}(\overline{u'^2} - \overline{v'^2})\right]}_{D_{22}} \underbrace{-\frac{2}{\rho}\overline{v'\frac{\partial p'}{\partial r}}}_{\Pi_{22}} \underbrace{-4\Omega\overline{u'v'}}_{C_{22}} - \underbrace{2\nu\left[\overline{\left(\frac{\partial v'}{\partial\theta} - u'\right)^2}\frac{1}{r^2} + \overline{\left(\frac{\partial v'}{\partial r}\right)^2} + \overline{\left(\frac{\partial v'}{\partial z}\right)^2}\right]}_{\varepsilon_{22}} \tag{15}$$

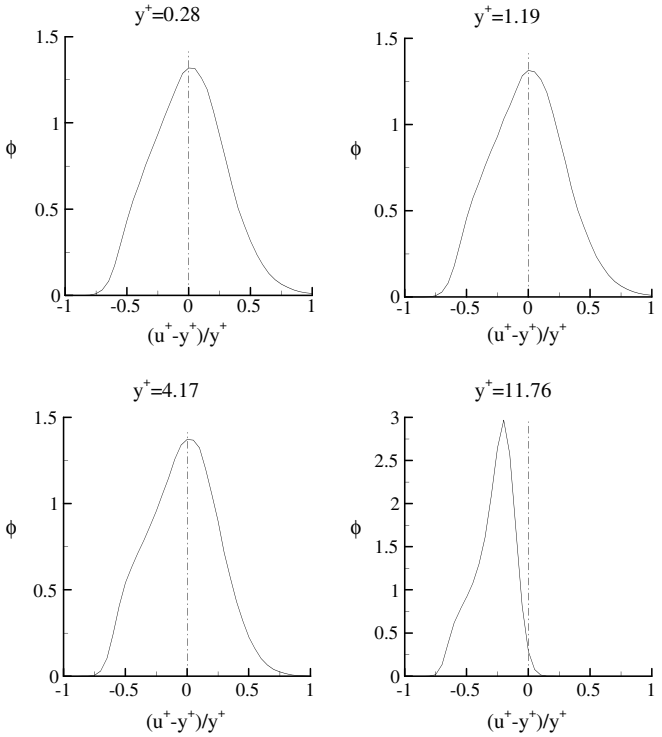

Fig. 16. Probability density function of departure from linearity of the streamwise velocity at $Re_R^* = 348$ near the wall.

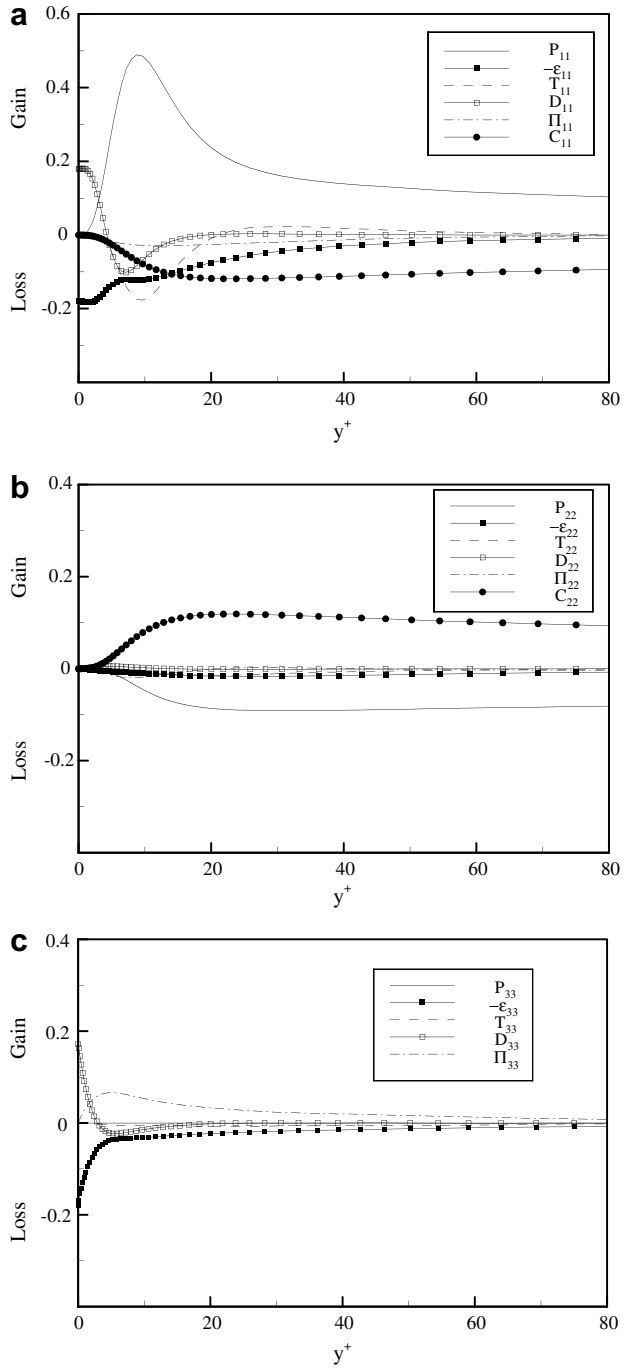

Fig. 17. Budgets of Reynolds normal stress components: (a) streamwise, (b) wall normal and (c) spanwise.

$$\overline{w'^2}-\text{budget}$$

$$0=\underbrace{-\frac{1}{r}\frac{\partial r\overline{w'w'v'}}{\partial r}}_{T_{33}}+\underbrace{\nu\frac{1}{r}\frac{\partial}{\partial r}\left(r\frac{\partial\overline{w'w'}}{\partial r}\right)}_{D_{33}}\underbrace{-\frac{2}{\rho}\overline{w'\frac{\partial p'}{\partial z}}}_{\Pi_{33}}$$
$$\underbrace{-2\nu\left[\overline{\left(\frac{\partial w'}{\partial\theta}\right)^2}\frac{1}{r^2}+\overline{\left(\frac{\partial w'}{\partial r}\right)^2}+\overline{\left(\frac{\partial w'}{\partial z}\right)^2}\right]}_{\varepsilon_{33}}. \quad (16)$$

The k budget has already been discussed by Hwang et al. (2007) who noted the effect of the Coriolis components, C_{11} and C_{22} in Eqs. (14) and (15) which affect the production of u' and v'. C_{11} is seen as a loss in Fig. 17a while C_{22} is seen as a gain in Fig. 17b.

Production of v' is seen from Fig. 17b to be negative thus leaving C_{22} as the only significant positive term. It is interesting to note that in fully developed channel and pipe flows, the production term in the v' budget is zero so that this budget component can only lead to redistribution and dissipation of fluctuation energy whereas in the present case, an additional mechanism is introduced whereby energy is extracted from u' by the C_{11} term, fed into the v' component only to be returned to the u' by half of the P_{22} component through P_{11}. The remaining part of P_{22} represents negative production and acts against C_{22}. This process represents an addition to the process described by Rotta (1962) for turbulent boundary layers as "Longitudinal velocity fluctuations exist because of the simultaneous existence of the Reynolds shear stress and mean velocity gradient, transverse and lateral velocity fluctuations exist because of the pressure fluctuations, and the Reynolds shear stress exists because of the simultaneous existence of transverse velocity fluctuations and mean velocity gradient". Production of w' is dominated by the pressure term, Fig. 17c, except in the wall region where diffusion also becomes a significant source term.

4.10. Normal surface stresses (wall pressure fluctuation)

Mechanical effects in flow affected corrosion can include normal surface stresses in addition to the shear stresses discussed above. Such failure can be due to fatigue of the surface film, especially if a soft zone exists between it and the solid surface thus making the protective film pliable. Statistical characteristics of surface pressure fluctuations are therefore required.

The spatial extent of pressure fluctuations as given by azimuthal and spanwise correlations, Fig. 18a and b, compared with

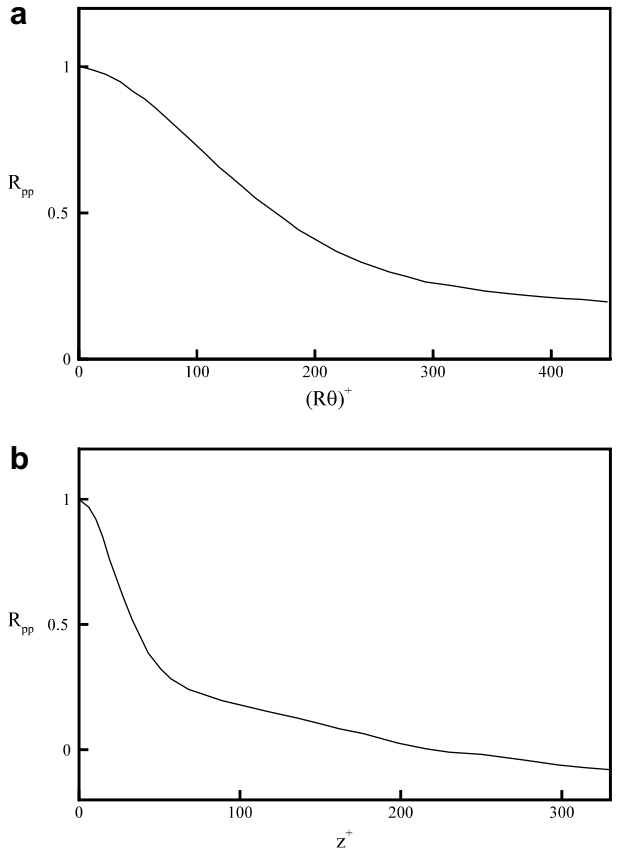

Fig. 18. Spatial correlations of wall pressure fluctuations, (a) streamwise separation and (b) spanwise separation.

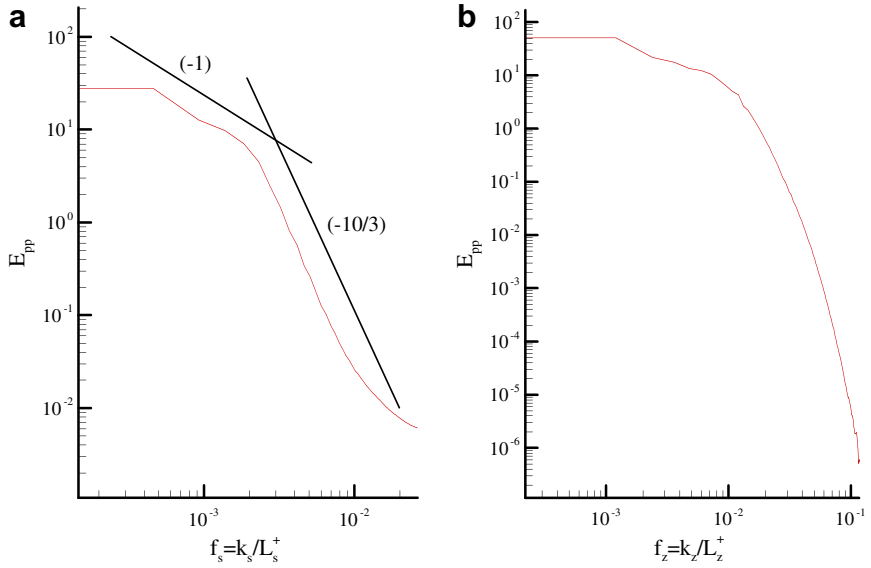

Fig. 19. Spectra of wall pressure fluctuations, (a) streamwise and (b) spanwise.

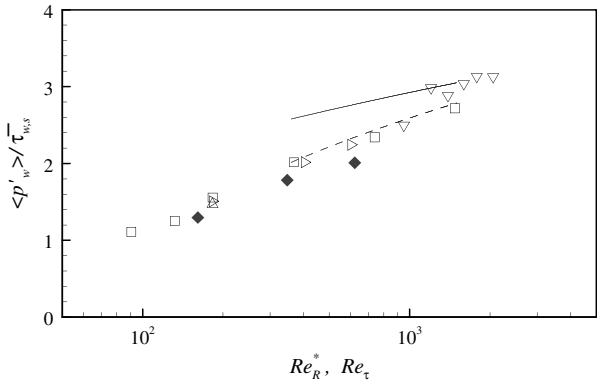

Fig. 20. Variations in rms values of wall pressure fluctuation: ♦, current result; □, DNS of channel flow by Hu et al. (2006); ▽, experimental result of turbulent boundary layer by Farabee and Casarella (1991); ▷, DNS of channel flow by Moser et al. (1999); △, DNS of channel flow by Kim et al. (1987); ————, formula of Farabee and Casarella (1991); - - - - - - - -, formula of Hu et al. (2006).

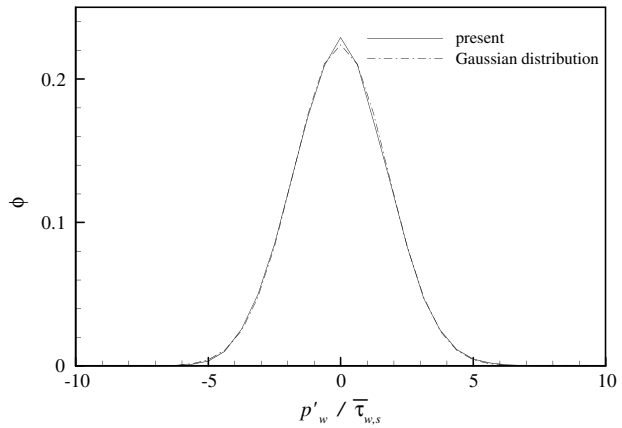

Fig. 21. Probability density function for the wall pressure fluctuation at $Re_R^* = 348$.

corresponding correlations of the fluctuating velocities available in Hwang et al. (2007), shows much greater correlation lengths. This result is to be expected as the wall pressure fluctuations include not only pressure fluctuations of the nearby scales but also those due to the very largest scales existing in the flow (Hinze, 1975).

Table 3
Skewness and Kurtosis of wall pressure fluctuation

Re_R^*	Skewness	Kurtosis
161	−0.38	2.90
348	0.06	3.05
623	0.24	3.78

Pressure fluctuation spectra of Fig. 19 were computed from the corresponding spatial correlations of Fig. 18. Spectra show a distinct difference relative to the wall shear stress fluctuations, Fig. 5, in the region of maximum energy contribution. Included in Fig. 19 are lines representing the (−1) and (−10/3) drop offs found in flat plate boundary layers attributed to Willmarth and Yang (1970). The (−1) region represents the energy containing part of the spectrum and is seen to agree closely with that for flat plate boundary layers as does the spectral drop off at the higher wavenumbers.

In Fig. 20, the current rms values of wall pressure fluctuation are presented together with those of other authors for channel flow and boundary layer flow. Correlations proposed by Hu et al. (2006) for channel flow and by Farabee and Casarella (1991) for turbulent boundary layer flow are also shown. It is seen that the current rms values are only slightly lower than those for the other flow configurations. Hinze, 1975 suggests a ratio of rms of pressure fluctuations to mean streamwise wall shear stress of 3.0 for boundary layers. The present data lie below this value but like the other data in Fig. 20, tend toward a value of 3.0 as Reynolds number increases. Consequently, Coriolis forces in the present flow do not seem to have an effect on this ratio.

For a statistical model of possible surface damage to corrosion films, it is necessary to know the distribution of likely pressure forces which consist of the mean and fluctuating parts. From Fig. 21 it is seen that the probability density function for the middle Reynolds number tested is similar to a Gaussian distribution but the data of Table 3 indicate that skewness and flatness (kurtosis) increase with Reynolds number thus indicating increasingly larger fluctuation extremes.

5. Concluding remarks

Flow around a rotating circular cylinder such as used for corrosion studies has been found to differ from non-rotating geometries with negligible streamline curvature due to the effect of Coriolis forces on the turbulent velocity field. Coriolis forces have no effect on the mean field other than to lower the constant in the logarithmic expression commonly used to relate the non-dimensional velocity profile to distance from the wall. The slope of this expression is still the inverse of the von Karman constant when velocity is expressed relative to the moving wall.

The turbulent velocity field is changed by a reduction in the streamwise velocity fluctuation relative to the other two fluctuating velocity components. The net effect is to make the streamwise and spanwise fluctuating wall shear stresses nearly identical in magnitude, spectral behaviour and probability densities. Budgets of velocity fluctuation energy show the role played by Coriolis forces which lead to radial transfer of momentum resulting in an energy production term in the Reynolds stress budget for the radial velocity component which does not exist in non-rotating geometries with negligible streamline curvature.

Extremes of fluctuating wall shear stresses and wall normal pressure fluctuations have been quantified and found to be significantly higher than the mean wall shear stress. This requires consideration when considering damage probability of protective films on surfaces. As for non-rotating geometries with negligible streamline curvature, no wall shear stress reversals were detected. The fluctuating pressure field was found to be correlated over larger lengths than the fluctuating velocities.

For flow modelling purposes it has been shown that the turbulent kinetic energy is a good approximation to the total wall shear stress fluctuation energy. This will allow the latter to be predicted by turbulence models, if these predict the turbulent kinetic energy within the wall region with good accuracy. Corrosion models based on total wall shear stress are then feasible without having to resort to direct numerical simulation of high Schmidt number flows to obtain corrosion predictions. As these models rely on the assumption that the diffusion layer lies within the viscous sublayer with linear velocity profile, probability density distributions at various y^+ are given to show that velocity profiles are indeed linear within the region of $y^+ < 5$.

Acknowledgement

This work was financially supported by UVRC, Korea.

References

Bremhorst, K., Kear, G., Keating, A.J., Huang, S.-H., 2005. Patch and whole of surface mass-transfer rate measurements on a stepped rotating cylinder electrode. Corrosion 61 (10), 968–975.

Colella, K.J., Keith, W.L., 2003. Measurements and scaling of wall shear stress fluctuations. Experiments in Fluids 34 (2), 253–260.

Darby, N.A., Newton, C.J., Sharman, J.D.B., 1999. Simulations of Bayer liquor pipeflows using a rotating cylinder electrode. Light Metals, 87–94.

Dierich, M., Gersten, K., Schlottmann, F., 1998. Turbulent flow around a rotating cylinder in a quiescent fluid. Experiments in Fluids 25, 455–460.

Eisenberg, M., Tobias, C.W., Wilke, C.R., 1954. Ionic mass transfer and concentration polarization at rotating electrodes. Journal of the Electrochemical Society 101 (6), 306–320.

Farabee, T.M., Casarella, M.J., 1991. Spectral features of wall pressure fluctuations beneath turbulent boundary layers. Physics of Fluids A 3 (10), 2410–2420.

Gabe, D.R., 1974. The rotating cylinder electrode. Journal of Applied Electrochemistry 4 (2), 91–108.

Gabe, D.R., Walsh, F.C., 1983. The rotating cylinder electrode: a review of development. Journal of Applied Electrochemistry 13 (1), 3–21.

Gabe, D.R., Wilcox, G.D., Gonzalex-Garcia, J., Walsh, F.C., 1998. The rotating cylinder electrode: its continued development and application. Journal of Applied Electrochemistry 28 (8), 759–780.

Hanratty, T.J., Campbell, J.A., 1996. Measurements of wall shear stress. In: Goldstein, R.J. (Ed.), Fluid Mechanics Measurements. Taylor and Francis, Washington, DC, pp. 575–648. Chapter 9.

Haut, B., Ben-Amor, H., Coulon, L., Jacquet, A., Halloin, V., 2003. Hydrodynamics and mass transfer in a Couette-Taylor bioreactor for the culture of animal cells. Chemical Engineering Science 58, 777–784.

Hinze, J.O., 1975. Turbulence. McGraw-Hill, New York.

Hu, Z.W., Morfey, C.L., Sandham, N.D., 2006. Wall pressure and shear stress spectra from direct simulations of channel flow. AIAA Journal 44 (7), 1541–1549.

Hwang, J.-Y., Yang, K.-S., Bremhorst, K., 2007. Direct numerical simulation of turbulent flow around a rotating circular cylinder. Journal of Fluids Engineering 129, 40–47.

Jacobs, C., Qin, Z., Bremhorst, K., 2006. Comparison of RANS modelling with DNS and experimental data for a converging–diverging nozzle and a rotating cylinder electrode. In: Schwarz, P. (Ed.), Fifth International Conference on CFD in the Process Industries. CSIRO, Melbourne, Australia.

Jeon, S., Choi, H., Yoo, J.Y., 1999. Space–time characteristics of the wall shear–stress fluctuations in a low Reynolds-number channel flow. Physics of Fluids 11 (10), 3084–3094.

Kasagi, N., Hirata, M., 1975. Transport Phenomena in Near-Wall Region of Turbulent Boundary Layer Around a Rotating Cylinder. ASME Proceedings 75-WA/HT-58.

Kim, J., Moin, P., Moser, R.D., 1987. Turbulence statistics in fully developed channel flow at low Reynolds number. Journal of Fluid Mechanics 177, 133–166.

Kristoffersen, R., Andersson, H.I., 1993. Direct simulations of low-Reynolds-number turbulent flow in a rotating channel. Journal of Fluid Mechanics 256, 163–197.

Launder, B.E., Tselepidakis, D.P., Younis, B.A., 1987. A second-moment closure study of rotating channel flow. Journal of Fluid Mechanics 183, 63–75.

Levich, V.G., 1962. Physicochemical Hydrodynamics. Prentice-Hall Inc., New Jersey.

Lezius, D.K., Johnston, J.P., 1976. Roll-cell instabilities in rotating laminar and turbulent channel flows. Journal of Fluid Mechanics 77, 153–175.

Moser, R.D., Kim, J., Mansour, N.N., 1999. Direct numerical simulation of turbulent channel flow up to $Re_t = 590$. Physics of Fluids 11 (4), 943–945.

Nesic, S., Postlethwaite, J., 1990. Relationship between the structure of disturbed flow and erosion corrosion. Corrosion 46 (11), 874–880.

Nesic, S., Solvi, G.T., Enerhaug, J., 1995. Comparison of the rotating cylinder and pipe flow tests for flow-sensitive carbon dioxide corrosion. Corrosion 51 (10), 773–787.

Nesic, S., Solvi, G.T., Skjerve, S., 1997. Comparison of rotating cylinder and loop methods for testing CO_2 corrosion inhibitors. British Corrosion Journal 32 (4), 269–276.

Pettersson, B.A., Andersson, H.I., Hjelm-Larsen, O., 1996. Analysis of near-wall second moment closures applied to flows affected by streamline curvature. In: Rodi, W., Bergeles, G. (Eds.), Engineering Turbulence Modelling and Experiments 3. Elsevier.

Pletcher, D., Walsh, F.C., 1993. Industrial Electrochemistry. Blackie Academic and Professional, London.

Rosenfeld, M., Kwak, D., Vinkur, M., 1994. A fractional step solution method for the unsteady incompressible Navier–Stokes equations in generalized coordinate systems. Journal of Computational Physics 94, 102–137.

Rotta, J.C., 1962. Turbulent boundary layers in incompressible flow. Progress in Aeronautical Science 2 (1), 1–95.

Silverman, D.C., 1988. Rotating cylinder electrode–geometry relationships for prediction of velocity-sensitive corrosion. Corrosion – NACE 44 (1), 42–49.

Silverman, D.C., 2003. Simplified equation for simulating velocity-sensitive corrosion in the rotating cylinder electrode at higher Reynolds numbers. Corrosion 59 (3), 207–211.

Theodorsen, T., Reiger, A., 1944. Experiments on Drag of Revolving Disks, Cylinders and Streamline Rods at High Speeds. National Advisory Committee for Aeronautics, Langley Field, Va. pp. 367–384.

Wild, P.M., Djilali, N., Vickers, G.W., 1996. Experimental and computational assessment of windage losses in rotating machinery. Journal of Fluids Engineering 118 (1), 116–122.

Willmarth, W.W., Yang, C.S., 1970. Wall-pressure fluctuations beneath turbulent boundary layers on a flat plate and a cylinder. Journal of Fluid Mechanics 41 (1), 47–80.

Yang, K.-S., Hwang, J.-Y., Bremhorst, K., Nesic, S., 2003. Numerical investigation of turbulent flow around a rotating stepped cylinder for corrosion study. The Canadian Journal of Chemical Engineering 81 (1), 26–36.